Research Article | Vol. 11, No. 12 / 1 December 2020 / Biomedical Optics Express 6945

Biomedical Optics EXPRESS

Quantitative multi-contrast *in vivo* mouse imaging with polarization diversity optical coherence tomography and angiography

Destiny Hsu,[1,5] Ji Hoon Kwon,[1,5] Ringo Ng,[1] Shuichi Makita,[2] Yoshiaki Yasuno,[2] Marinko V. Sarunic,[1] and Myeong Jin Ju[1,3,4,*]

[1] *Simon Fraser University, Biomedical Optics Research Group, Department of Engineering Science, Burnaby, British Columbia, Canada*
[2] *University of Tsukuba, Computational Optics Group, Institute of Applied Physics, Japan*
[3] *University of British Columbia, Department of Ophthalmology and Visual Sciences, Vancouver, British Columbia, Canada*
[4] *University of British Columbia, School of Biomedical Engineering, Vancouver, British Columbia, Canada*
[5] *co-first author*
[*] *myeongjin.ju@ubc.ca*

Abstract: Retinal microvasculature and the retinal pigment epithelium (RPE) play vital roles in maintaining the health and metabolic activity of the eye. Visualization of these retina structures is essential for pre-clinical studies of vision-robbing diseases, such as age-related macular degeneration (AMD). We have developed a quantitative multi-contrast polarization diversity OCT and angiography (QMC-PD-OCTA) system for imaging and visualizing pigment in the RPE using degree of polarization uniformity (DOPU), along with flow in the retinal capillaries using OCT angiography (OCTA). An adaptive DOPU averaging kernel was developed to increase quantifiable values from visual data, and QMC *en face* images permit simultaneous visualization of vessel location, depth, melanin region thickness, and mean DOPU values, allowing rapid identification and differentiation of disease symptoms. The retina of five different mice strains were measured *in vivo*, with results demonstrating potential for pre-clinical studies of retinal disorders.

© 2020 Optical Society of America under the terms of the OSA Open Access Publishing Agreement

1. Introduction

Non-invasive retinal imaging techniques and methods are essential for both clinical and preclinical vision research to aid the development of novel therapies for irreversible vision loss. To undertake controlled and rapid examination into the pathological aspects of human retinal disorders, small animal models have been employed extensively in pre-clinical studies [1–6]. *In vivo* imaging modalities ubiquitous in human clinical care, including optical coherence tomography (OCT), are readily adapted for small animal imaging, thus enabling longitudinal research and reducing the number of subjects required per study [7–11]. Additionally, the availability of a wide selection of transgenic strains allows for targeted investigation of disease mechanisms, with customized models, such as very low density lipoprotein receptor (VLDLR) and RPE65 mice, tailored to express specific human pathologies or desired biomarkers, permitting controlled examination of retinal degeneration and physiological responses to dysfunction [11–13].

Of the physical factors relating to vision loss, the retinal pigment epithelium (RPE) plays a vital role in sustaining retinal health. The RPE is a strongly scattering mono-layer of cells located immediately anterior to the choroid that plays a key role in the metabolic cycle of the photoreceptor layer. [14–16]. Many research reports suggest that vision-robbing disorders, such as retinitis pigmentosa (RP) and age-related macular degeneration (AMD), are highly correlated

#403209 https://doi.org/10.1364/BOE.403209
Journal © 2020 Received 22 Jul 2020; revised 15 Oct 2020; accepted 31 Oct 2020; published 6 Nov 2020

Biomedical Optics EXPRESS

to functional failure of the RPE, making studies of the layer of significant interest amongst ophthalmologists and vision researchers [17–21]. The RPE and choroid layers are populated by melanin granules, which inherently exhibit polarization-scrambling properties. As a functional extension of OCT, polarization-sensitive OCT (PS-OCT) has led to the adoption of polarization diversity detection (PDD), permitting the acquisition of degree of polarization uniformity (DOPU) contrast. This contrast is capable of leveraging the intrinsic polarization-scrambling property of the melanin granules in these regions, facilitating selective layer identification for targeted morphological RPE examination [22–28].

For full investigation of disorders and their effects on retinal physiology, the use of multiple tissue-specific imaging contrast mechanisms is essential in pathological research. While imaging modalities exist in isolation to provide specific tissue or layer contrasts, multi-contrast imaging, with proper compositing of the contrasts into a single image, provides valuable context for retinal features, health, and degradation, in relation to each other. Selective RPE imaging provides further benefits through integration with OCT angiography (OCTA); in cases of neovascularization, tracing the origin of new vessel growth complements the diagnosis of diabetic retinopathy and AMD [13]. Other methods exploring multi-contrast imaging have experimented with combined OCTA with DOPU contrast, such as multi-functional OCT [11] and pigment-and-flow imaging [28]. However, there remains need for visualizations of simultaneous vascular and structural information relative to the RPE, which are key features in various disorders and require strategic compositions of the contrasts for meaningful visual evaluation.

In our previously published work [27], we introduced our multi-scale and multi-contrast OCT system, capable of imaging pigment in the RPE as well as flow in the retinal capillaries using OCTA. For this study, we have modified this previous setup and adapted it for small animal imaging, using rodent models to validate extensions to our signal and image processing algorithms, creating a polarization diversity OCT and angiography (PD-OCTA) system. In the present report, we introduce an adaptive DOPU averaging kernel, with separable coordinate averaging and rotational variation to conform to melanin-rich structures of the retina, avoiding overestimation of DOPU boundaries and better reflecting retinal physiology. We used DOPU contrast for RPE layer structural mapping, combining this information with OCTA in the quantification of vessel depths with respect to the RPE. This method aids in highlighting neovascularization and new vessel growth, as well as simultaneous display of melanin migration, retinal lesions, and RPE thinning, integrating multiple symptom markers into a single *en face* image. Using these quantities, we have produced quantitative multi-contrast (QMC) *en face* projections, displaying depth-encoded retinal vessel networks on melanin region maps, quantifying melanin concentration and thickness in the RPE and choroid regions to create a unified data map that characterizes both functional vascular information and structural RPE integrity. System performance was verified with multiple rodent models exhibiting variations in melanin concentration and retinal pathologies, with our results demonstrating its capability to visualize and characterize each based on their quantified measurements.

2. Methods

2.1. System

Figure 1 presents the layout of the system employed in this study. A commercially-available MEMS-based short cavity wavelength swept laser (Axsun Technology Inc.) with a scanning frequency of 100 kHz, a center wavelength of 1060 nm and a full width half maximum (FWHM) of 85 nm was used as a light source. The system is comprised of three main units: OCT interferometer, phase calibration unit, and PDD unit. The detailed description of the phase calibration and the PDD units can be found in Ref. [27].

The OCT interferometer consisted of three single-mode fiber couplers. A custom-built retinal scanner designed for the small animal model was connected to the sample arm. The retinal

Biomedical Optics EXPRESS

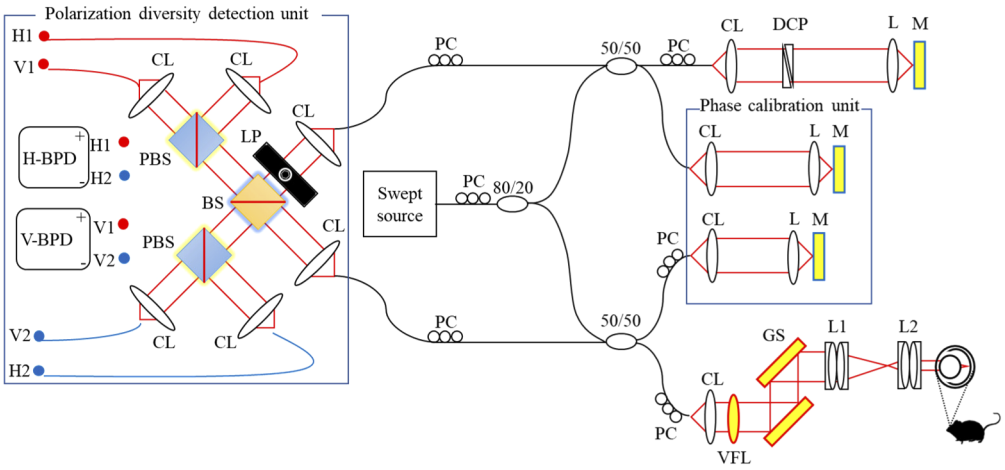

Fig. 1. Schematic of the QMC-PD-OCTA system. Polarization Controller (PC); Collimator (CL); Lens (L); Mirror (M); Dispersion Compensation Block (DCB); Galvanometer Scanner (GS); Variable Focus Lens (VFL); Linear Polarizer (LP); Beam Splitter (BS); Polarizing Beam Splitter (PBS); Balanced Photodetector (BPD); L1 = 2 × 200 mm, L2 = 2 × 125 mm.

scanner consisted of a fiber collimator (F240APC-1064, Thorlabs Inc., Newton, NJ, USA), a variable focus lens (VFL, A-39N-1, Corning, NY, USA), a two-axis galvanometer scanner (Compact 506, ScannerMax, FL, USA), and two optical relay lens sets. Two achromatic doublets (AC254-200-B, f_1 = 100 mm, and AC254-125-B, f_2 = 62.5 mm, Thorlabs Inc., Newton, NJ, USA) were used in the first and second optical relay as shown in Fig. 1. The numerical aperture (NA) of the system was measured to be 0.29, as defined by $NA = nd/2f$, where $n = 1.35$, d is the beam diameter incident on the cornea, measured to be1.1 mm ($1/e^2$), and f is the focal length of the mouse eye, taken as 2.6 mm [29]. The depth of focus (DOF) and nominal lateral resolution were calculated to be 16.05 µm and 1.86 µm respectively, as defined by $DOF = 4\lambda/\pi NA^2$ [30] and $\Delta x_{OCT} = 0.51\lambda/NA$ [31], where λ is the central wavelength. Dispersion mismatch in the OCT interferometer was compensated by inserting a dispersion compensation block (LSM05DC, Thorlabs Inc., Newton, NJ, USA) in the reference arm. Any remaining dispersion mismatch was corrected numerically in post-processing [32].

The OCT interference signal was digitized by a 12-bit waveform digitizer (ATS9350, AlazarTech Inc., Canada) with a 500 MHz sampling frequency and 1024 sampling points. The sampled interference signal was rescaled to the wavenumber domain using a pre-defined rescaling parameter obtained by a time-frequency calibration method [32]. The depth resolution defined by the −3 dB width was measured to be 8.7 µm in air (corresponding to the resolution of 6.4 µm in tissue with n=1.35), and the sensitivity measured at ∼1 mm depth was 92 dB at each polarization channel, with power of the incidental beam on the cornea measured at ∼1.0 mW. Because the signal energy is split into two OCT images for PDD, the sensitivity of the system measured for a single image is 3 dB lower than that of standard OCT. This fundamental sensitivity loss is overcome by the coherent composite method, discussed in Section 2.4.2 [24,25]. After considering the fundamental loss of the 50:50 fiber coupler, the shot-noise-limited sensitivity of a single channel became approximately −100 dB. The departure of the measured sensitivity from the shot-noise-limited sensitivity by −8 dB was accounted for by the single-pass transmittance of the sample arm, which has been measured to be −0.9 dB, the fiber coupling loss at the PDD, measured to be −3.4 dB, and possible recoupling loss at the fiber-tip in the scanning unit, due to misalignment of a mirror target during sensitivity measurement.

Biomedical Optics EXPRESS

2.2. Imaging protocol

Prior to imaging, mice were anesthetized with a subcutaneous injection of ketamine (100 mg/kg of body weight, average mouse weight 20–30 grams) and dexmedetomidine (0.1 mg/kg of body weight). Pupils were dilated using a single drop of 0.5% tropicamide, and a rigid 0-Diopter contact lens was used to keep the cornea hydrated during imaging. The mouse was placed in a custom-built stage with three-dimensional control, manually adjusted for imaging alignment.

High-contrast polarization sensitive imaging was obtained by adjusting the polarization controller, matching the intensity between H- and V-channel outputs. For *in vivo* mouse imaging, the focal plane was directed to the deep capillary plexus, allowing for optimized OCTA contrast with statistically minimal variation to DOPU contrast [27]. The transversal area of 1.2 mm (horizontal) × 1.2 mm (vertical) was scanned with 500 × 2000 A-scans in 10 seconds. In this scanning protocol, four repeated B-scans were taken at a single location, and used for intensity averaging for SNR-enhanced OCT images and OCTA images through measuring the variance of complex OCT signals [33].

2.3. Animal selection and handling

For validation of DOPU contrast measurements and diseased model visualization, rodent models were selected which exhibited quantifiable differences in melanin concentration as well as varying degrees of retinal pathology. The strains chosen to demonstrate varying melanin concentration were wild type B6 mice (C57BL/6J), serving as a baseline measurement, B6 agouti mice (C57BL/6J-A^{w-J}/J) for their lowered melanin production, and B6 albino mice (B6(Cg)-Tyr^{c-2J}/J) for their lack of melanin pigmentation [34]. To characterize models of various human pathologies with differing symptoms, wild type was used again as a healthy baseline population, with RPE65 mice (B6(A)-Rpe65^{rd12}/J) selected as a model for Leber's congenital amaurosis (LCA) due to retinal thinning and melanin migration to the choroid, and VLDLR mice (VLDLR^{tm1Her}/J) selected as a wet AMD model for their neovascularization and retinal lesions [10–12]. Details of all mice and strains are listed in Table 1.

Table 1. Details of all mouse models employed. Imaging sessions were divided into separate validation studies for melanin concentration variation and pathological symptom visualization.

	Wild Type	Agouti	Albino	RPE65	VLDLR
Mouse Strain	C57BL/6J	C57BL/6J-A^{w-J}/J	B6(Cg)-Tyr^{c-2J}/J	B6(A)-Rpe65^{rd12}/J	VLDLR^{tm1Her}/J
Number	3	2	3	3	2
Imaging Session	Melanin/				
Pathological	Melanin	Melanin	Pathological	Pathological	
Features	Baseline	Decreased melanin	Unpigmented	LCA model	Wet AMD model
Age	12 months	13 months	12 months	11 months	4 months
Symptom Stabilization	6 months	6 months	6 months	5 months	3 months

Mice roughly double the age of symptom stabilization were chosen for assured visibility of desired characteristics, as well as maintaining similar ages across strains for consistency. Ages ranged from 330 to 360 postnatal days, with the exception of VLDLR at 120 postnatal days. Symptoms in VLDLR rodents manifest earlier than other strains, as well as having higher tendency of developing cataracts with advanced age [13]. As such, the chosen VLDLR specimens were sufficiently stabilized for imaging suited to visualization of wet-type AMD.

All mice were purchased from Jackson Laboratory, ME, USA. Imaging was performed according to the protocols issued by the Canadian Council on Animal Care and with approval of the University Animal Care Committee at Simon Fraser University.

Biomedical Optics EXPRESS

2.4. QMC image processing pipeline

QMC image post-processing is characterized by two *en face* image generation stages; quantified melanin region contrast with DOPU quantities, and depth-resolved vessel contrast through OCTA. Figure 2 illustrates the image processing pipeline, modified from the previously-reported multi-contrast processing in order to improve the quantifiable results [27].

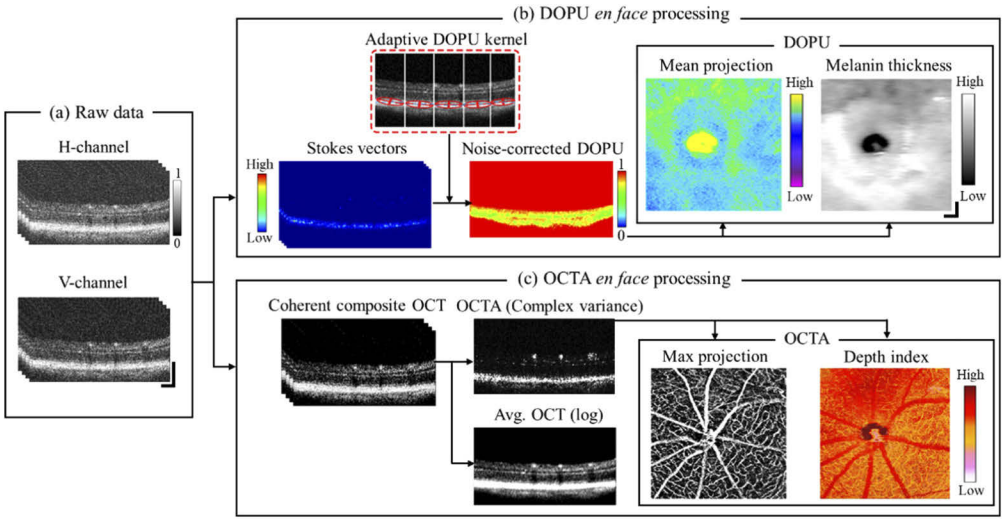

Fig. 2. Flowchart of QMC image processing pipeline. (a) Raw volumetric data from orthogonally polarized outputs, H- and V-channels. (b) DOPU *en face* image processing; generation of Stokes vectors, adaptive DOPU kernel averaging, noise-corrected DOPU, and melanin maps for mean DOPU value and melanin region thickness. (c) OCTA *en face* image processing; coherent composition of polarization channels, scattering intensity averaged OCT and OCTA, and OCTA *en face* maximum intensity projection image with corresponding depth indices relative to the RPE. Scalebars indicate 100 µm.

2.4.1. DOPU process with adaptive averaging kernel

Following data acquisition, volumes comprised of two orthogonally polarized channels, H- and V-channels, were obtained as illustrated in Fig. 2(a). The dual-channel output data was processed with a standard OCT pipeline, including automatic numerical dispersion compensation [35] and wavenumber resampling [32], in preparation for a noise-corrected DOPU generation algorithm [24]. DOPU contrast computed the circular variance of Stokes vectors in a local region, with the noise-corrected Stokes vector parameters $s_i(x,z,f)$, i = (0, 1, 2, 3) given as;

$$\begin{bmatrix} s_0(x,z,f) \\ s_1(x,z,f) \\ s_2(x,z,f) \\ s_3(x,z,f) \end{bmatrix} = \begin{bmatrix} |g_H(x,z,f)|^2 + |g_V(x,z,f)|^2 - [n_H(z) + n_V(z)] \\ |g_H(x,z,f)|^2 - |g_V(x,z,f)|^2 - [n_H(z) + n_V(z)] \\ 2Re[g_H(x,z,f)g_V^*(x,z,f)] \\ 2Im[g_H(x,z,f)g_V^*(x,z,f)] \end{bmatrix} \tag{1}$$

where f is the frame index within a repeated B-scan set (f = (1,2,. . . ,N), with N=4), $g_H(x,z,f)$ and $g_V(x,z,f)$ are the processed OCT H- and V-channel output data, *Re* and *Im* are the real and imaginary parts, $g_V^*(x,z,f)$ is the complex conjugate data, and $n_H(z)$ and $n_V(z)$ indicate the measured noise powers for each polarization channel. Noise levels were estimated as the

Biomedical Optics EXPRESS

variance of the vitreous region, since the noise floor is almost flat over the imaging depth range [24]. DOPU values were then calculated as;

$$DOPU(x,z) = \frac{\sum_{f=1}^{N} \sqrt{\sum_{v=1}^{3} \overline{s_v}^2(x,z,f)}}{\sum_{f=1}^{N} \overline{s_0}^2(x,z,f)} \tag{2}$$

where $\overline{s_v}$ is the spatially-averaged Stokes parameter [24,28]. Quantitative measurement of the melanin region via DOPU is frustrated by this local spatial averaging of region statistics, inherent in the calculation process. For high DOPU contrast and signal clarity, a larger kernel is preferred, but precise layer boundaries and small retinal features, such as lesions and drusen, risk blurring or obfuscation. However, smaller averaging kernels are insufficient to overcome background noise and fail to provide clear DOPU values.

To overcome the trade-off between DOPU contrast and sharpness, as well as enhance the resolution of these local spatial statistics, an adaptive DOPU averaging kernel was employed to compute the moving average in place of a traditional rectangular kernel. The computation performed by this averaging kernel is capable of adaptively conforming to the shape of retinal structures along B-scans, reducing overestimation of melanin boundaries and distortion of small melanin projections or detachments.

The design principles of the adaptive DOPU kernel relied on basic knowledge of the RPE and choroid structures with the following assertions:

- The bulk of depolarizing deposits in the eye will be in these pigmented layers.
- These layers will remain relatively continuous across the eye with the exception of the optic nerve head (ONH), where these layers are absent.
- Traces of melanin pigments near the ONH manifest as depolarizing signals at this location. These are remnants from development of the hyaloid canal [36], which can be excluded from our analysis of the RPE/choroid by cropping.
- All other retinal tissue can be characterized as non-depolarizing tissue [36].

After calculation of the Stokes vector parameters, exclusion of the ONH was accomplished by simple cropping at the mean depth of the nerve fiber layer, ignoring points above this line. The number of points in each A-line should be consistent for each B-scan, but the precise number N of points was inconsequential to calculations and can vary between scans. Each B-scan was processed with the adaptive DOPU averaging kernel algorithm outlined in Fig. 3.

a. Separation into slices

For feature-specific adaptive averaging, B-scans were first divided into continuous segments of approximately 100 A-lines. This step permitted kernels to be fitted to the orientation of the curvature of the layer and melanin structures on the order of ~240 µm. The precise number of A-lines are adjustable for different applications and OCT setups, and was set to 100 for validation of the methods presented here. Volumes should ideally be cropped to reduce amount of non-retinal signal present for more economic data size.

b. Least-squares elliptical fitting and angle extraction

Each slice's largest retinal structure was estimated with an ellipse by least-squares fitting to determine directionality, as illustrated in the red dotted lined inset of Fig. 2(b). The ellipse form was selected using the knowledge that these deposits would form elongated

Biomedical Optics EXPRESS

shapes along the XZ-plane or small projections into the Z-plane. A collection of n ellipses was created, with the function for the ellipse corresponding to the nth slice given as;

$$E_n = Ellipse_n(a, b, x_c, z_c) = \frac{(x - x_c)^2}{a^2} + \frac{(z - z_c)^2}{b^2} = 1 \tag{3}$$

with a as the semi-major axis, b as the semi-minor axis, (x, z) as the coordinates on the ellipse, and (x_c, z_c) as the coordinates of the centroid.

Prior to estimating the angle, thresholding by Otsu's method [37] was applied to the individual Stokes vector B-scans to separate background noise from visible retina feature data. For least-squares fitting within the given ellipsoid parameters, the equation to be minimized was the distance to the orthogonal contact point between the gradient of the nearest point lying on the ellipse and the target test point, as shown in Eq. (4).

$$\frac{\delta z}{\delta x}\frac{(z_i - z)}{(x_i - x)} = \frac{-b^2 x}{a^2 z}\frac{(z_i - z)}{(x_i - x)} = -1 \tag{4}$$

These conditions set a non-linear least-squares fitting function, which was solved using the Gauss-Newton method on the Jacobian matrices of each orthogonal contact point [38]. With the estimated semi-major axis a for ellipse E_n, the corresponding angle α_n to the x-axis is then found with simple trigonometry.

c. 1-D axial kernel filtering

The adaptive kernel was separated into two 1-D components, which were rotated in the XZ-plane according to angle α_n normal to the major axis of the slice ellipse E_n. This rotation ensured averaging was performed perpendicular to the retinal structure, reducing blurring between layers and calculating statistics of a more homogenous region of tissue. Averaging was first performed by 2-D convolution of the axial kernel across the nth slice, smoothing noise and estimating local spatial parameters in the axial direction. To avoid clipping at slice boundaries, the edges were padded through inclusion of additional A-lines, double the length of the axial kernel, which were cropped upon recombination into the full B-scan.

d. 1-D lateral kernel filtering

The noise-corrected axially filtered slices were subsequently processed with the lateral kernel, rotated parallel to the major axis with α_n, and the same padding method applied as in step (c). This kernel served to estimate the local statistics for each retinal layer, therefore rotation was necessary to reduce contributions from neighbouring layers, providing increased continuity and lessening boundary blurring.

e. Cropping and stitching slices

Before the final output, the padding A-lines are cropped from each slice and then recombined, producing the final averaged B-scan with the same dimensions as the input.

The final output of the adaptive DOPU averaging kernel was a smoothed Stokes vector B-scan $\overline{s'_v}$, replacing $\overline{s_v}$ in Eq. (1) for further steps of DOPU calculation. Obtained DOPU quantities were subsequently thresholded and smoothed by a three-dimensional median filter (3 × 3 × 3 pixels) for removal of any remaining background noise. For the purposes of this study, DOPU averaging kernel sizes of 3 (axial) × 5 (lateral) pixels corresponding to ~10 µm × 10 µm were used for optimal image quality, determined experimentally. However, ideal kernel size may vary depending on OCT protocols and system parameters, and further testing may be required to evaluate the standard ideal size for rodent eyes.

Biomedical Optics EXPRESS

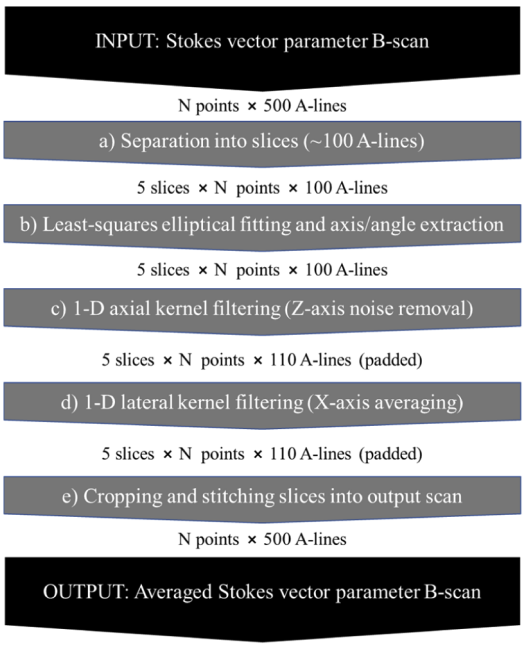

Fig. 3. Flowchart of adaptive DOPU averaging kernel process, taken for a data volume of N cropped axial points and 500 lateral A-lines.

2.4.2. Full QMC *en face* image generation

The noise-corrected, adaptively-averaged DOPU B-scans were used to extract the melanin-containing regions of the RPE and choroid through simple thresholding of the background level, due to the inherent depolarization of the melanin granules in the layers exhibiting DOPU values roughly < 0.95, found empirically. Due to the simple thresholding, segmentation was performed faster than traditional graph cut methods; a common 4-core CPU (Intel i5-7600, 3.50 GHz, 16.0 GB RAM) using MATLAB 2017b required 3 seconds per B-scan, including DOPU calculations and adaptive kernel processing. Moreover, since segmentation was based on an intrinsic tissue property, it was insensitive to morphological changes in the layer structure and tolerant of abnormalities in the RPE.

Mean DOPU value was calculated on an A-line basis, taken along the depth of the melanin region values, mapping pink and blue to lower DOPU values indicating areas of higher melanin concentration, and yellow to higher DOPU values corresponding with lower melanin concentration. Thickness was equivalently calculated as the largest continuous region of melanin presence along each depth, and was mapped linearly to an intensity gradient, with black corresponding to zero thickness and white to the average thickness value for a healthy rodent eye (approximately 55 pixels, or ~200 µm, found experimentally). The final molecular melanin contrast region maps are shown in the final steps of Fig. 2(b).

Due to the use of PDD, the output was divided into two separate signals, resulting in an inherent loss in SNR. To maximize the SNR, as well as overcome this loss, the phase offset between the H- and V-channel data was estimated and compensated, allowing the summation of the two complex signals to form a polarization-insensitive coherent composite OCT [24,25]. From this coherent composite data, conventional OCT averaging and OCTA processing were performed using the multiple B-scan protocol. Signal-enhanced scattering contrast OCT was obtained through temporal averaging, and OCTA vessel contrast was obtained using complex variance estimation across each set of repeated B-scans, taken sequentially from the same transverse

Biomedical Optics EXPRESS

location [39,40]. The pixel indices of the vessels found via OCTA were cross-referenced with the corresponding location on the DOPU contrast map to extract their relative depth with respect to the RPE layer, which was subsequently colour-coded correspondingly to a healthy rodent's retinal vascular network, with orange corresponding to the deep capillary plexus depth, red for the superficial capillary plexus, and white-pink for suspicious vessel growth in the outer nuclear layer. Figure 2(c) displays the processing steps and resulting location and depth maps from the OCTA process.

With the *en face* maps obtained in Fig. 2(b) and (c), QMC imaging is capable of simultaneous display of four contrasts which quantify both vascular and molecular data; OCTA, vessel depth, melanin region mean DOPU values, and melanin region thickness. Figure 4 illustrates the full QMC *en face* image generation process. For melanin region map generation, the mean DOPU value contrast map was multiplied with the melanin region thickness map, thus encoding the region thickness in the melanin values by the intensity of the background, as seen in Fig. 4(a). Equivalently, for OCTA *en face* image generation, the map of vessel locations was multiplied with the depth-encoded contrast map, colour-coding each vessel with their corresponding depth with respect to the RPE layer, as seen in Fig. 4(b). Figure 4(c) presents the resulting QMC *en face* image after overlaying the depth-encoded OCTA on the melanin region map, resulting in simultaneous display of all contrasts; OCTA position and depth in conjunction with RPE structure and thickness.

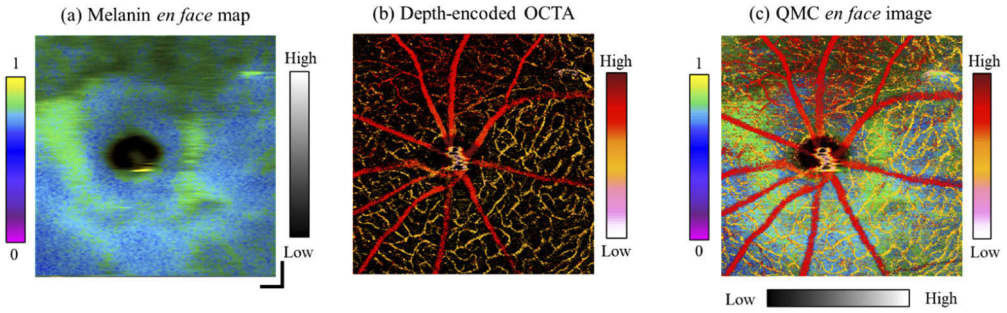

Fig. 4. QMC full *en face* image generation, contrast illustration. (a) Melanin region *en face* map of mean DOPU value with thickness map. (b) OCTA *en face* map of vessel location and depth with respect to the RPE. (c) Full QMC *en face* image displaying four contrasts simultaneously. Scalebars indicate 100 µm.

3. Results

3.1. QMC melanin concentration analysis

To visualize and validate the correlation between DOPU contrast and melanin, three separate mouse strains (WT, agouti and albino) were selected and imaged which exhibit different retinal melanin concentrations. Figure 5 shows a representative QMC-PD-OCTA image set for the selected strains, displayed in order of highest melanin concentration (WT) to lowest (albino).

Each of the specimens selected were chosen for exhibiting healthy vessel density and distribution, as shown in all three *en face* images, with red superficial capillary plexus and orange deep capillary plexus. This ensured that the sole variation in QMC *en face* images between strains was limited to the melanin region, postulated to be corresponding to regions of low DOPU value. To aid in fully characterizing the source of anomalous melanin deposits or vessels, composite DOPU B-scans were generated by multiplying DOPU contrast with the log-scaled OCT intensity signal, as seen in the top of Fig. 5. This allowed low DOPU regions to be spatially referenced

Biomedical Optics EXPRESS

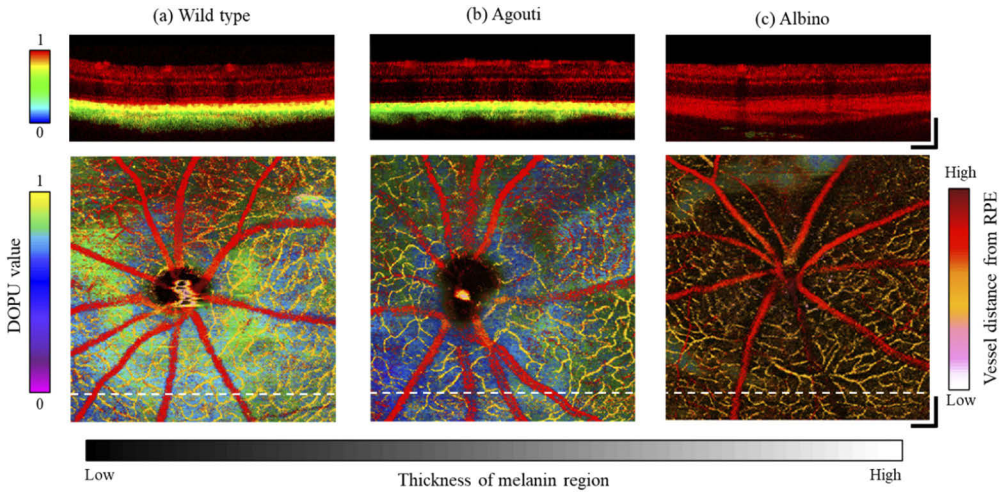

Fig. 5. Composite B-scans (top) and QMC *en face* images (bottom) of three rodent strains with differing melanin concentrations; (a)WT mouse; (b) Agouti mouse; (c) Albino mouse. Scalebars indicate 100 µm.

to non-depolarizing retinal structures, permitting easier differentiation between structural RPE features (such as lesions) or neovascularization from choroidal vasculature.

The QMC image shown in Fig. 5(a) displays the measured DOPU with colouration varying from green to blue, indicative of DOPU values characterising moderate to high melanin concentration. These colours are displayed with high brightness and saturation, signifying a thick melanin region of a healthy RPE and choroid with normal melanin distribution, which correlates with the WT strain. The composite B-scan shown in Fig. 5(a) also supports these results, with both the RPE and choroid region highlighted by low DOPU values and hence high melanin content. Regions surrounding the RPE and choroid lack depolarizing deposits, showing no lesions or melanin migration into the inner retina, further indicative of the health of this specimen.

In Fig. 5(b), DOPU values remain comparable in colour distribution and variation to Fig. 5(a), but the overall intensity and brightness are lowered, indicating fewer low DOPU values and thus a reduction in melanin distribution and the thickness of the melanin region. The corresponding composite B-scan also shows the RPE and choroid layers highlighted by low DOPU values, however the region is thinner than that of Fig. 5(a), and also displays slightly lower values in blue, suggesting that the melanin present is highly concentrated in a thinner region. This corresponds with the agouti mouse strain, as a characteristic of the phenotype is lowered melanin production compared to WT.

To further verify that DOPU is a measure of the polarization-scrambling of melanin granules and not the intensity of the RPE alone, the final *en face* image from the pigment-free albino mouse in Fig. 5(c) displays a background that is nearly black, indicating a lack of depolarizing deposits. Additionally, in spite of a bright RPE layer in the composite B-scan of this strain, there are no regions of low DOPU, with the entire retina displayed as uniformly red, polarization-preserving tissue, indicating a lack of melanin in the albino mouse eye.

To quantify the values found for all imaged specimens of each strain, a histogram displaying the percent distribution of all melanin region thickness values is shown in Fig. 6. Of the three strains, the distribution of WT lies at the highest measured thickness values. The center of the agouti strain's distribution is shifted to the lower end of the WT distribution, revealing their lowered melanin production. The entirety of the albino strain's distribution lies at thickness values below both other strains, supporting the albino's near complete lack of melanin. All

Biomedical Optics EXPRESS

zero thickness values were truncated for clarity to visualize the three strains simultaneously, as almost 99% of the thickness values in the albino mice were zero, severely distorting the graph and making inter-strain comparison difficult.

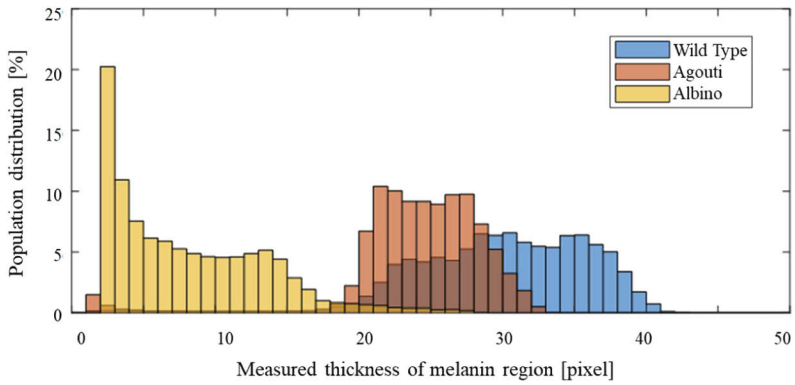

Fig. 6. Histogram of melanin region thickness distributions for all imaged mice, categorized by strain (WT, Agouti, Albino). Zero thickness values for albino mice have been neglected for ease of inter-strain display and comparison.

3.2. QMC pathological case visualization

For pathological case investigation using QMC imaging, three mouse strains (WT, RPE65 and VLDLR) were selected to model different human pathologies with distinct symptoms, with imaging results displayed in Fig. 7.

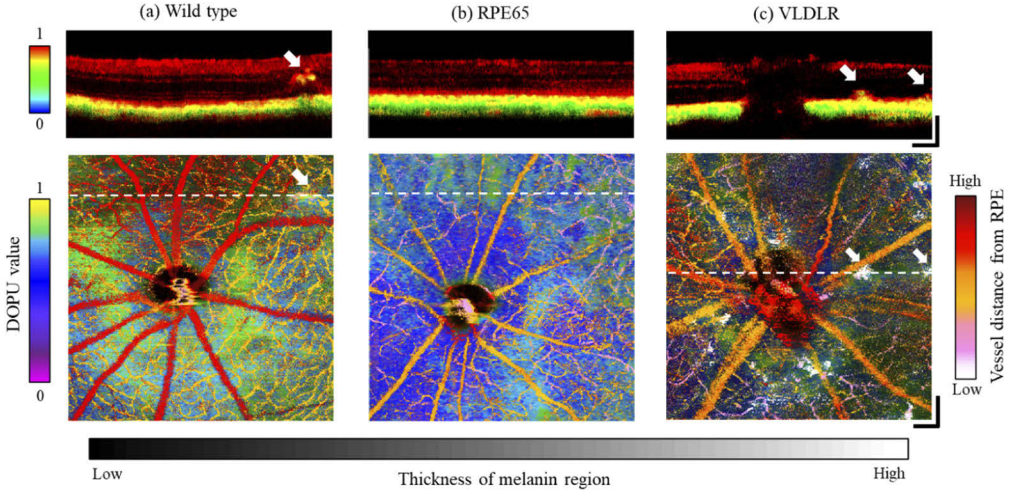

Fig. 7. Composite B-scans (top) and QMC *en face* images (bottom) of three different pathological case rodent strains; (a) WT mouse; (b) RPE 65 mouse; (c) VLDLR mouse. Scalebars indicate 100 µm.

The WT strain was initially selected as a healthy baseline example. However, one specimen was found to exhibit a case of a hyper-reflective focus (HPF), potentially due to melanin migration into the inner retina, a phenomenon also observed in Alzhiemer's studies using this strain as a control [41]. This HPF is indicated in the e*n face* image of Fig. 7(a) by brighter DOPU colour saturation,

Biomedical Optics EXPRESS

signifying an elevated RPE projection, as well as pink-toned vessels, signifying vessels abnormally in proximity to the RPE. The deposit itself is highlighted in the corresponding composite B-scan by the low DOPU value compared to surrounding tissue, suggesting migration of RPE cells into the inner retinal layers. This instance demonstrates the ability for QMC-PD-OCTA to visualize and detect anomalous features in an otherwise healthy population.

The RPE65 mouse lacks RPE65 enzyme (isomerohydrolase) expression in the RPE layer, resulting in retinal degeneration highly indicative of LCA [10,12]. Through the *en face* image for the RPE65 strain in Fig. 7(b), this is visualized by the proximity of the entire vessel network to the RPE, far closer than in a healthy eye, as the superficial plexus is at the depth of a proper deep plexus in orange, whereas the deep plexus is now located where the ONL should be in pink. Additionally, melanin migration to the choroid is also visible through the intense blue coloration of the background DOPU signal, indicating much higher levels of melanin in the outer retina compared with the other strains.

As a model for wet-type AMD, the VLDLR mouse is known to express choroidal neovascularization, RPE degeneration, and retinal lesions [11,13]. All these symptoms are visible in the *en face* image of Fig. 7(c), where the mouse eye displays white vessels indicative of neovascularization, darkened DOPU background signal with varying vessel depths, signifying a degraded and uneven RPE, and retinal lesions also creating falsely proximate white vessels. The ambiguity of the white proximate vessels is clarified through the composite B-scan, revealing two such 'vessels' to be retinal lesions, both indicated by the corresponding white arrows.

For further investigation and analysis of these pathological cases, circumpapillary plots were created from each strain, with measured values of the ONL layer thicknesses extracted from the calculated QMC data, displayed in Fig. 8.

Circumpapillary plots, computed as the average of five concentric radial scans, were taken from each rodent around the ONH as indicated in Fig. 8(a). These cross-sections were displayed for each strain (WT, RPE65, and VLDLR) in Fig. 8(b), with the white arrows indicating span of the measurements for the ONL, and the black arrows for measurements of the melanin region thickness, extracted using the DOPU measurements of the upper and lower boundaries of the low DOPU region in conjunction with OCTA values for the deep capillary plexus. A plot of the calculated ONL layer thickness values, determined as the distance between upper RPE boundary and deep capillary plexus, is displayed in Fig. 8(c). The corresponding melanin thickness, extracted as the low DOPU region depth range, is shown for the same rodents in Fig. 8(d), colour-coded for each strain. Owing to their respective retinal degeneration pathologies, both RPE65 and VLDLR have a relatively thinner ONL, as seen by their lower values compared to WT in Fig. 8(c). However, the graph of their respective melanin distributions in Fig. 8(d) demonstrates the difference in their disorders, revealing RPE degeneration specifically in VLDLR, whereas WT and RPE65 have comparable melanin region values. These results agree with previous research on the physiology of these strains, and present various means of distinguishing symptoms for proper diagnosis of pathologies.

3.3. Adaptive kernel comparison

Representative results for a healthy rodent eye are displayed at each step of the DOPU algorithm in Fig. 9. After generation of the Stokes vector parameters for a single B-scan (Fig. 9(a)), the averaging kernel was applied, followed by calculation of DOPU values, filtering background levels, and averaging across repeated B-scans to obtain the final DOPU B-scan (Fig. 9(b-c) left and center). The optional step of compositing DOPU with averaged OCT scans is also displayed (Fig. 9(b-c) right), visualizing DOPU with respect to retinal structures. The resulting melanin map projections, showing mean value and thickness values, are displayed for each kernel method in Fig. 9(d).

Biomedical Optics EXPRESS

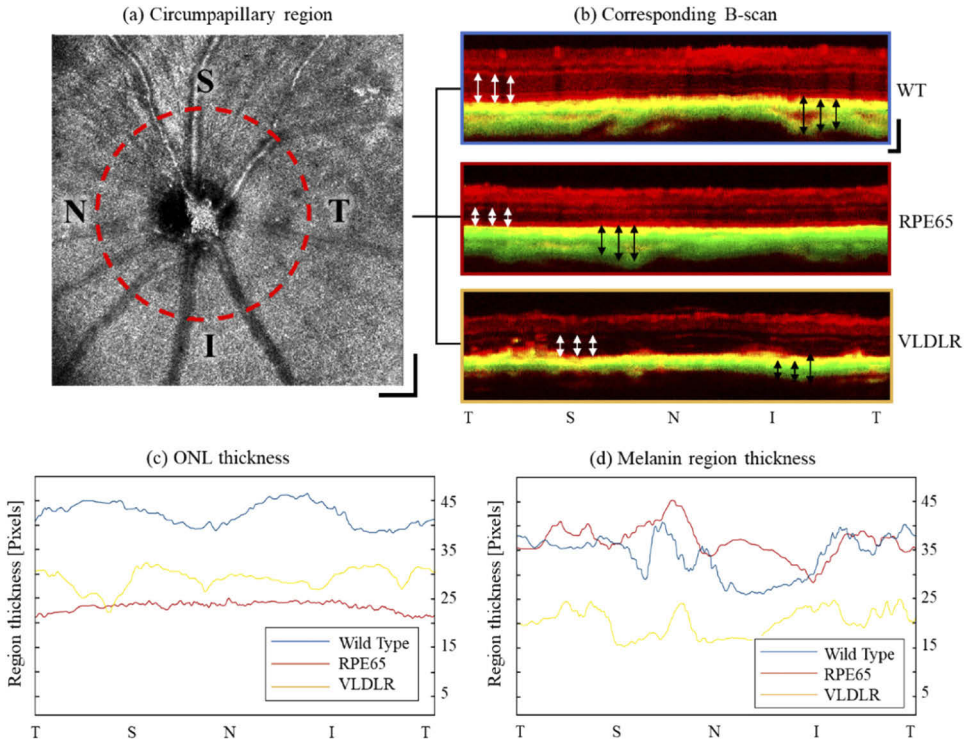

Fig. 8. Circumpapillary plot of three pathological rodent strains (WT, RPE65, VLDLR). (a) OCT *en face* view indicating the location of the averaged cross-sectional area. T, temporal; N, nasal; S, superior; I, inferior. (b) Composite DOPU circumpapillary B-scans of WT (top), RPE65 (center) and VLDLR (bottom), sampling depths for ONL and melanin region thicknesses indicated by white and black arrows, respectively. (c) ONL thickness plot. (d) Melanin region thickness plot. Scalebars indicate 100 µm.

The same volume was processed with both rigid (Fig. 9(b)) and adaptive kernels (Fig. 9(c)). As seen in Fig. 9(b), with rigid kernel processing, the upper and lower melanin boundaries appear ragged, and the region slightly enlarged. In comparison, the same frame processed with an adaptive DOPU kernel in Fig. 9(c), displays distinct region boundaries with increased continuity and reduced blurring, as well as remaining confined to the corresponding RPE and choroid structures in the composite B-scan. As a result, different distribution patterns were observed between the melanin map projections when processed with rigid versus adaptive kernels. The adaptive kernel-based projection image (Fig. 9(d), right) shows a more homogenous melanin distribution, with relatively consistent colouration of the mean DOPU value over the entire FOV, compared to the rigid kernel-based projection image (Fig. 9(d), left) showing higher delineation between the green and blue regions.

Retinal QMC images acquired from a VLDLR mouse were processed in the same manner, with a B-scan containing a lesion selected for analysis of adaptive kernel performance, shown in Fig. 10. From the QMC *en face* image displayed in Fig. 10(a), (a) B-scan was extracted from the location indicated by the dotted line, selected for its large cluster of white anomalous signal, circled in white. As shown in the DOPU B-scans of Fig. 10(b), this cluster signified a retinal lesion projecting from the RPE layer, displayed both with the DOPU in isolation (left) and with respect to the retinal layers in the composite DOPU B-scan (right). The top row displays DOPU values of the lesion processed with a rigid kernel, and the bottom displays the same location with

Biomedical Optics EXPRESS

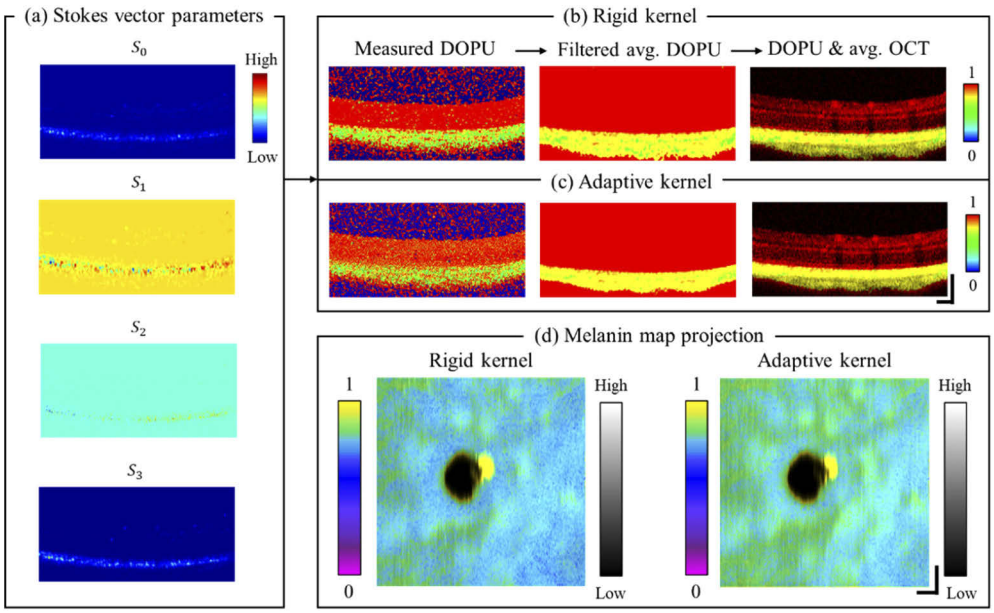

Fig. 9. Comparison of processed DOPU with adaptive and rigid kernel methods. (a) Stokes vector parameters for a single B-scan. DOPU B-scan processing (measured DOPU, filtering and averaging, composite DOPU B-scan) with (b) rigid and (c) adaptive kernels. (d) Melanin map projections computed with rigid and adaptive kernels. Scalebars indicate 100 µm.

an adaptive kernel process, where the white arrows indicate small features of the lesion and the choroid which are rendered sharper through the adaptive kernel process.

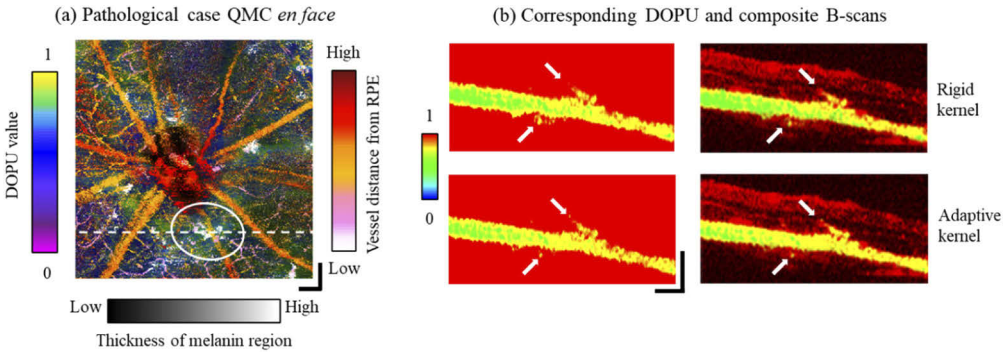

Fig. 10. Comparison of rigid and adaptive DOPU averaging kernels on pathological data. (a) QMC *en face* image of a VLDLR rodent eye, B-scan selected at dotted line with retinal lesion circled in white. (b) DOPU (left) and composite DOPU B-scans (right) showing a VLDLR retinal lesion, processed with rigid (top) and adaptive (bottom) kernels. Arrows indicate features sharpened with the adaptive kernel. Scalebars indicate 100 µm.

4. Discussion

DOPU measurement presents variation of polarization properties between neighbouring points, and therefore each DOPU value represents statistical information from a local spatial average [24–26]. This necessitates that an integral element of DOPU calculation be devoted to spatial

Biomedical Optics EXPRESS

averaging, traditionally via a rigid rectangular convolutional kernel, which leads to trade-offs between higher contrast and retinal feature sharpness.

For the proposed QMC process, accurate and dependable measurements of the melanin region boundary were necessary to produce quantifiable data. With DOPU calculation employing a rectangular averaging kernel, overestimation of these boundaries was a frequent shortcoming, particularly in cases of retinal curvature or tilt and small features in the RPE. This becomes more pronounced in pathological eyes, as disturbances in the RPE structure may manifest in small deformations of the layer, which may be come blurred or lost in traditional DOPU rigid kernel averaging. Our adaptive DOPU averaging kernel was developed to overcome this limitation and diminish the trade-off between DOPU contrast and resolution, reducing the loss of clinical features for proper compositing with additional contrasts. While further validation with histology and collaboration with vision scientists is required to fully describe the utility of this method, results suggest potential for greater fidelity to retinal layer physiology and an increased ability to precisely visualize subtle symptoms of RPE degeneration.

As a high-dimensional imaging modality, QMC processing forms a composite of multiple contrasts with minimal obstruction between the values, giving information-dense visual data. Melanin concentration is presented without occlusion by RPE and choroid thickness variation through coding each parameter in two separate features, DOPU colour and brightness. The depth-encoded OCTA map directly displays the three-dimensional vessel distribution in the inner retina, while simultaneously serving as an indirect measure of ONL degeneration, characterized by a reduction in distance between the vasculature and the RPE, displayed via a shift in colour values. Capturing multiple pathological aspects in imaging data serves as an aid in interpreting disease effects on vasculature and RPE simultaneously, while compositing all the contrasts in a single QMC *en face* image allows for rapid extraction of this information without additional averaging and registration required.

This study employed mouse models to validate our methodology for multi-dimensional image composition and visualization of retinal pathologies. Nevertheless, as the optical design was modified from a human imaging system, repurposing and restoring the setup and algorithm for human studies is a simple step. In the future, QMC imaging can be employed in human pre-clinical investigation of disease mechanisms, serving as a direct and intuitive means of detecting pathological impact on a patient's vasculature, RPE and choroid *in vivo*, providing a direct means of visualizing the effects of retinal disorders on multiple important biomarkers from a single image.

5. Conclusion

In this study, we have presented an extension to multi-contrast OCT imaging, building upon previously reported methods to integrate preclinically-relevant quantifiable features in a single QMC *en face* image. Our QMC-PD-OCTA system was modified to permit small animal imaging, using transgenic mice as models for human retinal pathologies for validation of our methodology. With our QMC processing algorithm, we presented results differentiating mouse strains of varying retinal melanin concentrations, demonstrating the ability of DOPU to detect and selectively visualize melanin granules in the RPE and choroid as well as the QMC *en face* image to visualize these changes. We investigated our adaptive kernel process for improved quantification of DOPU values, as well as a novel method of compositing multiple contrasts into one image. Using this methodology, we can provide multiple information to image operators and investigators intuitively, providing all contrasts in a single imaging domain, thus giving a clearer picture of the inter-relations of disease mechanisms during diagnosis and disease investigation. Additionally, through the use of three rodent models of human pathologies, we presented QMC images and measured retinal layer thicknesses which corresponded to melanin migration, LCA, and wet-type AMD, with results demonstrating the ability of QMC to highlight characteristic symptoms of

Biomedical Optics EXPRESS

each, lending potential for use in pre-clinical studies for investigation and development of novel treatments for various retinal disorders.

Funding

Canadian Institutes of Health Research; Natural Sciences and Engineering Research Council of Canada.

Disclosures

MVS: Seymour Vision (I). SM, YY: Yokogawa Electric Corp. (F), Nikon (F), Kao Corp. (F), Topcon (F), Tomey Corp (F, P), Sky Technology (F).

References

1. S. M. Petersen-Jones, "Animal models of human retinal dystrophies," Eye **12**(3), 566–570 (1998).
2. G. J. Chader, "Animal models in research on retinal degenerations: Past progress and future hope," Vision Res. **42**(4), 393–399 (2002).
3. G. Huber, S. C. Beck, C. Grimm, A. Sahaboglu-Tekgoz, F. Paquet-Durand, A. Wenzel, P. Humphries, T. Michael Redmond, M. W. Seeliger, and M. Dominik Fischer, "Spectral domain optical coherence tomography in mouse models of retinal degeneration," Invest. Ophthalmol. Visual Sci. **50**(12), 5888–5895 (2009).
4. D. J. Wahl, Y. Jian, S. Bonora, R. J. Zawadzki, and M. V. Sarunic, "Wavefront sensorless adaptive optics fluorescence biomicroscope for in vivo retinal imaging in mice," Opt. Express **7**(1), 1 (2016).
5. P. Zhang, A. Zam, Y. Jian, X. Wang, Y. Li, K. S. Lam, M. E. Burns, M. V. Sarunic, E. N. Pugh, and R. J. Zawadzki, "In vivo wide-field multispectral scanning laser ophthalmoscopy–optical coherence tomography mouse retinal imager: longitudinal imaging of ganglion cells, microglia, and Müller glia, and mapping of the mouse retinal and choroidal vasculature," J. Biomed. Opt. **20**(12), 126005 (2015).
6. D. J. Wahl, M. Cua, S. Lee, Y. Zhao, R. J. Zawadzki, S. Bonora, Y. Jian, and M. V. Sarunic, "Two photon imaging of mouse retina with sensorless adaptive optics," *2016 IEEE Photonics Conf. IPC 2016*, 130–131 (2017).
7. M. E. Pennesi, M. Neuringer, and R. J. Courtney, "Animal models of age related macular degeneration," Mol. Aspects Med. **33**(4), 487–509 (2012).
8. M. Al-Sheikh, N. A. Iafe, N. Phasukkijwatana, S. R. Sadda, and D. Sarraf, "Biomarkers of Neovascular Activity in Age-related Macular Degeneration Using Optical Coherence Tomography Angiography," Retina **38**(2), 220–230 (2018).
9. M. M. Castillo, G. Mowatt, A. Elders, N. Lois, C. Fraser, R. Hernández, W. Amoaku, J. M. Burr, A. Lotery, C. R. Ramsay, and A. Azuara-Blanco, "Optical coherence tomography for the monitoring of neovascular age-related macular degeneration: A systematic review," Ophthalmology **122**(2), 399–406 (2015).
10. R. Tanabu, K. Sato, N. Monai, K. Yamauchi, T. Gonome, Y. Xie, S. Takahashi, S. Ishiguro, and M. Nakazawa, "The findings of optical coherence tomography of retinal degeneration in relation to the morphological and electroretinographic features in RPE65 −/− mice," PLoS One **14**(1), e0210439 (2019).
11. M. Augustin, S. Fialová, T. Himmel, M. Glösmann, T. Lengheimer, D. J. Harper, R. Plasenzotti, M. Pircher, C. K. Hitzenberger, and B. Baumann, "Multi-functional OCT enables longitudinal study of retinal changes in a VLDLR knockout mouse model," PLoS One **11**(10), e0164419 (2016).
12. R. C. Caruso, T. S. Aleman, A. V. Cideciyan, A. J. Roman, A. Sumaroka, C. L. Mullins, S. L. Boye, W. W. Hauswirth, and S. G. Jacobson, "Retinal disease in Rpe65-deficient mice: Comparison to human leber congenital amaurosis due to RPE65 mutations," Invest. Ophthalmol. Visual Sci. **51**(10), 5304–5313 (2010).
13. M. Augustin, M. Wechdorn, U. Pfeiffenberger, T. Himmel, S. Fialová, R. M. Werkmeister, C. K. Hitzenberger, M. Glösmann, and B. Baumann, "In vivo characterization of spontaneous retinal neovascularization in the mouse eye by multifunctional optical coherence tomography," Invest. Ophthalmol. Visual Sci. **59**(5), 2054–2068 (2018).
14. V. L. Bonilha, M. E. Rayborn, S. K. Bhattacharya, X. Gu, J. S. Crabb, W. Crabb, and J. G. Hollyfield, "The Retinal Pigment Epithelium Apical Microvilli and Retinal Function," Adv. Exp. Med. Biol. **572**, 519–524 (2006).
15. D. N. Hu, J. D. Simon, and T. Sarna, "Role of ocular melanin in ophthalmic physiology and pathology," Photochem. Photobiol. **84**(3), 639–644 (2008).
16. M. Boulton and P. Dayhaw-Barker, "The role of the retinal pigment epithelium: Topographical variation and ageing changes," Eye **15**(3), 384–389 (2001).
17. S. M. Gu, D. A. Thompson, C. R. S. Srikumari, B. Lorenz, U. Finckh, A. Nicoletti, K. R. Murthy, M. Rathmann, G. Kumaramanickavel, M. J. Denton, and A. Gal, "Mutations in RPE65 cause autosomal recessive childhood-onset severe retinal dystrophy," Nat. Genet. **17**(2), 194–197 (1997).
18. S. Beatty, M. Boulton, D. Henson, H. H. Koh, and I. J. Murray, "Macular pigment and age related macular degeneration," Br. J. Ophthalmol. **83**(7), 867–877 (1999).
19. D. A. Thompson and A. Gal, "Genetic defects in vitamin A metabolism of the retinal pigment epithelium," Dev. Ophthalmol. **37**, 141–154 (2003).

Biomedical Optics EXPRESS

20. A. Pyakurel, D. Balmer, M. K. Saba-El-Leil, C. Kizilyaprak, J. Daraspe, B. M. Humbel, L. Voisin, Y. Z. Le, J. von Lintig, S. Meloche, and R. Roduit, "Loss of Extracellular Signal-Regulated Kinase 1/2 in the Retinal Pigment Epithelium Leads to RPE65 Decrease and Retinal Degeneration," Mol. Cell. Biol. **37**(24), e00295 (2017).
21. M. Lapierre-landry, J. Carroll, and M. C. Skala, "Imaging retinal melanin : a review of current technologies," J. Biol. Eng. **5**, 29 (2018).
22. E. Götzinger, M. Pircher, W. Geitzenauer, C. Ahlers, B. Baumann, S. Michels, U. Schmidt-Erfurth, and C. K. Hitzenberger, "Retinal pigment epithelium segmentation by polarization sensitive optical coherence tomography," Opt. Express **16**(21), 16410–16422 (2008).
23. C. Ahlers, E. Götzinger, M. Pircher, I. Golbaz, F. Prager, C. Schütze, B. Baumann, C. K. Hitzenberger, and U. Schmidt-Erfurth, "Imaging of the retinal pigment epithelium in age-related macular degeneration using polarization-sensitive optical coherence tomography," Invest. Ophthalmol. Visual Sci. **51**(4), 2149–2157 (2010).
24. S. Makita, Y.-J. Hong, M. Miura, and Y. Yasuno, "Degree of polarization uniformity with high noise immunity using polarization-sensitive optical coherence tomography," Opt. Lett. **39**(24), 6783 (2014).
25. M. J. Ju, Y.-J. Hong, S. Makita, Y. Lim, K. Kurokawa, L. Duan, M. Miura, S. Tang, and Y. Yasuno, "Advanced multi-contrast Jones matrix optical coherence tomography for Doppler and polarization sensitive imaging," Opt. Express **21**(16), 19412 (2013).
26. B. Baumann, S. O. Baumann, T. Konegger, M. Pircher, E. Götzinger, F. Schlanitz, C. Schütze, H. Sattmann, M. Litschauer, U. Schmidt-Erfurth, and C. K. Hitzenberger, "Polarization sensitive optical coherence tomography of melanin provides intrinsic contrast based on depolarization," Biomed. Opt. Express **3**(7), 1670–1683 (2012).
27. M. J. Ju, D. Hsu, J. H. Kwon, D. J. Wahl, S. Bonora, Y. Jian, S. Makita, Y. Yasuno, and M. V. Sarunic, "Multi-scale and -contrast sensorless adaptive optics optical coherence tomography," J. Biomed. Opt. **22**(12), 1–10 (2019).
28. S. Makita, T. Mino, T. Yamaguchi, M. Miura, S. Azuma, and Y. Yasuno, "Clinical prototype of pigment and flow imaging optical coherence tomography for posterior eye investigation," Biomed. Opt. Express **9**(9), 4372 (2018).
29. Y. Geng, L. A. Schery, R. Sharma, A. Dubra, K. Ahmad, R. T. Libby, and D. R. Williams, "Optical properties of the mouse eye," Biomed. Opt. Express **2**(4), 717 (2011).
30. E. Bo, Y. Luo, S. Chen, X. Liu, N. Wang, X. Ge, X. Wang, S. Chen, S. Chen, J. Li, and L. Liu, "Depth-of-focus extension in optical coherence tomography via multiple aperture synthesis," Optica **4**(7), 701 (2017).
31. M. Pircher and R. J. Zawadzki, "Review of adaptive optics OCT (AO-OCT): principles and applications for retinal imaging [Invited]," Biomed. Opt. Express **8**(5), 2536–2562 (2017).
32. Y. Yasuno, V. D. Madjarova, S. Makita, M. Akiba, A. Morosawa, C. Chong, T. Sakai, K.-P. Chan, M. Itoh, and T. Yatagai, "Three-dimensional and high-speed swept-source optical coherence tomography for in vivo investigation of human anterior eye segments," Opt. Express **13**(26), 10652 (2005).
33. J. Xu, S. Song, Y. Li, and R. K. Wang, "Complex-based OCT angiography algorithm recovers microvascular information better than amplitude- or phase-based algorithms in phase-stable systems," Phys. Med. Biol. **63**(1), 015023 (2018).
34. R. K. Meleppat, P. Zhang, M. J. Ju, S. K. Manna, Y. Jian, E. N. Pugh, and R. J. Zawadzki, "Directional optical coherence tomography reveals melanin concentration-dependent scattering properties of retinal pigment epithelium," J. Biomed. Opt. **24**(06), 1–10 (2019).
35. Y. Yasuno, Y. Hong, S. Makita, M. Yamanari, M. Akiba, M. Miura, and T. Yatagai, "In vivo high-contrast imaging of deep posterior eye by 1-μm swept source optical coherence tomography and scattering optical coherence angiography," Opt. Express **15**(10), 6121 (2007).
36. B. Baumann, J. Schirmer, S. Rauscher, S. Fialová, M. Glösmann, M. Augustin, M. Pircher, M. Gröger, and C. K. Hitzenberger, "Melanin pigmentation in rat eyes: In vivo imaging by polarization-sensitive optical coherence tomography and comparison to histology," Invest. Ophthalmol. Visual Sci. **56**(12), 7462–7472 (2015).
37. N. Otsu, "A threshold selection method from gray-level histograms," IEEE Trans. Syst. Man Cybern. **9**(1), 62–66 (1979).
38. S. J. Ahn, W. Rauh, and H. J. Warnecke, "Least-squares orthogonal distances fitting of circle, sphere, elipse, hyperbola, and parabola," Pattern Recognit. **34**(12), 2283–2303 (2001).
39. H. R. G. W. Verstraete, M. Heisler, M. J. Ju, D. Wahl, L. Bliek, J. Kalkman, S. Bonora, Y. Jian, M. Verhaegen, and M. V. Sarunic, "Wavefront sensorless adaptive optics OCT with the DONE algorithm for in vivo human retinal imaging [Invited]," Biomed. Opt. Express **8**(4), 2261 (2017).
40. M. J. Ju, M. Heisler, A. Athwal, M. V. Sarunic, and Y. Jian, "Effective bidirectional scanning pattern for optical coherence tomography angiography," Biomed. Opt. Express **9**(5), 2336–2350 (2018).
41. D. J. Harper, M. Augustin, A. Lichtenegger, J. Gesperger, T. Himmel, M. Muck, C. W. Merkle, P. Eugui, S. Kummer, A. Woehrer, M. Glösmann, and B. Baumann, "Retinal analysis of a mouse model of Alzheimer's disease with multicontrast optical coherence tomography," Neurophotonics **7**(01), 1 (2020).